Type I fatty acid synthase (FAS) trapped in the octanoyl-bound state

Authors: Alexander Rittner, Karthik S. Paithankar, Aaron Himmler, and Martin Grininger*

Author affiliations: Institute of Organic Chemistry and Chemical Biology, Buchmann Institute for Molecular Life Sciences, Goethe University Frankfurt, Max-von-Laue-Str. 15, Frankfurt am Main, D-60438, Germany

*Corresponding author: grininger@chemie.uni-frankfurt.de

Telephone number: +49 69 798 42705

Abstract

De novo fatty acid biosynthesis in humans is accomplished by a multidomain protein, the type I fatty acid synthase (FAS). Although ubiquitously expressed in all tissues, fatty acid synthesis is not essential in normal healthy cells due to sufficient supply with fatty acids by the diet. However, FAS is overexpressed in cancer cells and correlates with tumor malignancy, which makes FAS an attractive selective therapeutic target in tumorigenesis. Herein, we present a crystal structure of the condensing part of murine FAS, highly homologous to human FAS, with octanoyl moieties covalently bound to the transferase (MAT) and the condensation (KS) domain. The MAT domain binds the octanoyl moiety in a novel (unique) conformation, which reflects the pronounced conformational dynamics of the substrate binding site responsible for the MAT substrate promiscuity. In contrast, the KS binding pocket just subtly adapts to the octanoyl moiety upon substrate binding. Besides the rigid domain structure, we found a positive cooperative effect in the substrate binding of the KS domain by a comprehensive enzyme kinetic study. These structural and mechanistic findings contribute significantly to our understanding of the mode of action of FAS and may guide future rational inhibitor designs.

Highlights

- The X-ray structure of the KS-MAT didomain of murine type I FAS is presented in an octanoyl-bound state.
- Multiple conformations of the MAT domain and a dynamic active site pocket explain substrate promiscuity.
- The rigid domain structure and minor structural changes upon acylation are in line with the strict substrate specificity of the KS domain.
- Enzyme kinetics reveals cooperativity in the KS-mediated transacylation step.

Keywords

fatty acid synthesis, multienzyme, condensation, transacylation, cooperativity, inhibition

Abbreviations

FAS, fatty acid synthase; MAT, malonyl-/acetyltransferase; ACP, acyl carrier protein; KS, β-ketoacyl synthase; KR, ketoreductase; DH, dehydratase; ER, enoylreductase; TE, thioesterase; LD, linker domain;

Introduction

Fatty acids are essential molecules in most living cells, serving as key compounds of cell membranes, as energy supply in the metabolism, as secondary messengers in signaling pathways or as covalent modifications to recruit proteins to membranes. They can either be obtained directly from the diet or are synthesized *de novo* by fatty acid synthases (FASs) from simple building blocks in repeating cyclic reactions. Although the chemistry of fatty acid synthesis is largely conserved across all kingdoms of life, the structural organization of the participating enzymes differs dramatically. FAS complexes occurring in plants, bacteria and in mitochondria, known as the type II, perform biosynthesis by a series of monofunctional separate enzymes (Beld et al., 2015; Chen et al., 2018; White et al., 2005). In contrast, the CMN group bacteria (*Corynebacterium*, *Mycobacterium*, and *Nocardia*), fungi and higher eukaryotes utilize type I FASs that integrate all enzymatic functions into large macromolecular assemblies (Grininger, 2014; Heil et al., 2019; Herbst et al., 2018; Maier et al., 2010). Fungal and CMN-bacterial FASs form up to 2.7-MDa $\alpha_6\beta_6$-heterododecameric barrel-like structures (Boehringer et al., 2013; Elad et al., 2018; Johansson et al., 2008; Leibundgut et al., 2007; Lomakin et al., 2007). The animal FASs, including human FAS, emerge from a separate evolutionary development and consist of two polypeptide chains assembling into a 540-kDa intertwined “X-shaped” homodimer (Maier et al., 2008).

In animals, including human beings, fatty acid biosynthesis commences with the transfer of an acetyl moiety from acetyl-coenzyme A (CoA) to the terminal thiol of the phosphopantetheine arm of the acyl carrier protein (ACP) domain catalyzed by the malonyl-/acetyltransferase (MAT)

64 domain (Figure 1A) (Smith and Tsai, 2007). After being passed on to the
65 active site cysteine of the β-ketoacyl synthase (KS) domain, a malonyl moiety
66 is loaded on the free ACP domain in a second MAT-mediated transfer
67 reaction. Upon delivery of the malonyl moiety, the KS domain catalyzes a
68 decarboxylative Claisen condensation reaction in which the KS-bound acetyl
69 and the ACP-bound malonyl moieties combine to an ACP-bound β-ketoacyl
70 intermediate. Subsequently, the β-keto group is sequentially modified by three
71 processing domains, the ketoreductase (KR), the dehydratase (DH) and the
72 enoylreductase (ER) using NADPH as a reducing agent. Typically, fatty acid
73 synthesis runs seven cycles to deliver a fully reduced ACP-bound acyl chain
74 of 16 carbon atoms, which is eventually released as palmitic acid by
75 hydrolysis via the thioesterase (TE) domain (Figure 1A).

76 The key domains in fatty acid synthesis are MAT, KS and ACP,
77 responsible for the selection of substrates, C-C bond formation and substrate
78 shuttling, respectively (**Figure 1**B). The MAT domain of murine type I FAS
79 shows broad substrate specificity and facilitates the synthesis of methyl-
80 branched, odd numbered and functionalized fatty acids by alternative
81 substrate selection (Buckner et al., 1978; Rittner et al., 2019; Rittner et al.,
82 2018; Smith and Stern, 1983). On the contrary, the KS domain possesses a
83 strict specificity for saturated acyl moieties with a low acceptance of β-keto
84 groups to guarantee biosynthesis of saturated fatty acids *in vivo* (Witkowski et
85 al., 1997). The ACP domain is loaded by the MAT and ACP does not impose
86 substrate specificity in this step. However, the interaction of ACP with other
87 domains is necessary for the progress of synthesis and the specificity of this

interaction can affect the product formation (Dodge et al., 2019; Rossini et al., 2018; Sztain et al., 2019).

Although FASs are ubiquitously expressed in all tissues, *de novo* biosynthesis of fatty acids occurs at low levels as the demand is usually met by the diet (Semenkovich et al., 1995; Uhlén et al., 2015). Despite adequate nutritional lipid supply, the FAS gene is overexpressed under pathological conditions, being associated with diseases like diabetes, obesity and cancer, and upregulation of FAS correlates with tumor malignancy (Gansler et al., 1997; Khandekar et al., 2011; Kuhajda, 2006; Menendez et al., 2009; Nguyen et al., 2010; Rashid et al., 1997). FAS has emerged as a very promising therapeutic target in tumorigenesis, because pharmacological FAS inhibitors induce tumor cell death by apoptosis whereas normal cells are resistant (Pandey et al., 2012). To date, several inhibitors, like cerulenin, GSK2194069 and orlistat, have been identified or developed that target the KS, KR and TE domain, respectively (Hardwicke et al., 2014; Pandey et al., 2012; Pemble et al., 2007). Remarkably, the compound TVB-2640 recently entered phase 2 clinical trials showing promising results in combinatorial anti-cancer therapies (Buckley et al., 2017; Dean et al., 2016).

Herein, we report the crystal structure of the murine KS-MAT didomain at 2.7 Å resolution with octanoyl moieties covalently bound in the KS and the MAT active sites. By comparison with structures of domains in apo-form as well as with the malonyl-bound MAT domain, we analyze structure-function relationships and correlate the conformational variability of the individual domains with their substrate specificities. Furthermore, by applying a continuous fluorometric assay, we reveal detailed mechanistic insight into the

113 cooperative behavior of the KS-mediated transacylation reaction. The results
114 of this study provide new insights into the key processes of substrate loading
115 and condensation in fatty acid synthesis and foster the development and
116 optimization of inhibitors with potential antineoplastic properties.
117

Results

Crystal structure of the KS-MAT didomain with bound octanoyl moieties

In order to gain structural insights into the molecular basis for the substrate ambiguity of the MAT domain and the strict substrate specificity of the KS domain of murine type I FAS, we aimed at trapping both KS and MAT domains in the octanoyl-bound enzyme state. Following an established protocol (Rittner et al., 2018), the purified murine KS-MAT didomain, sharing 87 % sequence identity to the condensing part of human FAS (Pappenberger et al., 2010), was crystallized and crystals were soaked with octanoyl-CoA (Figure S1). X-ray diffraction data were collected to a resolution of 2.7 Å, and the resulting structural model refined to R/R_{free} of 0.18/0.23 (Table 1). The asymmetric unit contains four polypeptide chains (A-D) arranged as two biological dimers interacting via the cleft between the KS and the linker domain (LD) (**Figure 2**A). In all four chains, the KS domain is modified with an octanoyl moiety yielding the octanoyl-enzyme covalent complex. Furthermore, in one polypeptide chain (chain D), an octanoyl group is covalently bound to S581 of the MAT domain and an additional octanoyl-CoA is non-covalently trapped in the MAT binding tunnel (Figure 2B). This finding confirms previous data showing that octanoyl-CoA can prime murine type I fatty acid synthesis and that the MAT domain can catalyze the transfer of octanoyl moieties (Rittner et al., 2019; Rittner et al., 2018).

General description of the octanoyl-bound MAT domain

The MAT domain engages fatty acid synthesis in selecting the CoA-ester substrates for product assembly. It is located at the edge of the condensing part of animal FAS and inserted into the KS fold via the linker domain (LD). The exposed position and the utilization of only 8.4 % of the solvent-accessible area for domain-domain interactions reflect a high structural independence from the FAS fold. The substrate-binding pocket is formed by a cleft between the α/β-hydrolase and the ferredoxin-like subdomains and extends to the active site located in the center of the domain. The function of the MAT domain is to shuttle acyl moieties via the active serine between CoA-ester substrates and the ACP domain following a ping-pong bi-bi mechanism. The catalytic key residues S581 and H683 form a catalytic dyad with S581 acting as nucleophile and H683 serving in acid-base catalysis (Paiva et al., 2018). The nucleophilicity of S581 is enhanced by a helix dipole-moment due to its positioning within a strand-turn-helix motif termed the nucleophilic elbow (Hol, 1985). A key residue for the bifunctional role of MAT is R606 located in helix 7, which interacts with the carboxylic group of extender substrates. The absence of the guanidinium group leads to altered substrate specificity (Rangan and Smith, 1997; Rittner et al., 2018).

Upon soaking protein crystals with octanoyl-CoA, we found that S581 in chain D is covalently modified with an octanoyl moiety and, furthermore, a molecule octanoyl-CoA is non-covalently attached to the substrate binding pocket (**Figure 2**B). The placement of both ligands was based on the feature-enhanced map (FEM) and later validated by a Polder map (Figure S2) (Afonine et al., 2015; Liebschner et al., 2017). The octanoyl chain of octanoyl-

S581 is located in a tunnel between the two subdomains created between residues P640, F682, V740 and P742 and extends to the protein's surface (**Figure 2**C). The octanoyl group of octanoyl-CoA points towards helix 10 of the α/β-hydrolase fold in a substrate binding pocket between the subdomains created by residues I610, L615, L680, A681, F682, H683, F686 and L739. Rangan and Smith (1997) reported that the R606A variant from rat FAS showed increased turnover rates for the transfer of octanoyl moieties (Rangan and Smith, 1997). Based on this, Bunkoczi and co-workers (Bunkoczi et al., 2009) placed a decanoyl chain in the human R606A-mutated MAT binding site by a simulated docking experiment and concluded that space for longer acyl chains is created in the mutant due to the absence of the side chain of residue R606. In our structure, the positions of the octanoyl chains are slightly different to that of the computationally docked decanoyl chain. Upon binding the octanoyl chain, the side chains of residues R606 and L680 rotate to form an extended binding cavity that can accommodate the larger substrate. This feature is likely responsible for the high transacylation rate of murine MAT for octanoyl moieties and may not be present in rat MAT according to docking data (Bunkoczi et al., 2009). Again deviating from rat FAS data (Rangan and Smith, 1997), the murine MAT loses the capability for efficient transacylation of the octanoyl moiety upon mutation of R606 to alanine (Table 2).

Intriguingly, in the MAT-octanoyl-CoA complex, the nucleobase of octanoyl-CoA is bound at a specific position between the two subdomains with the adenine stacked between side chains of F671 and R773. Besides the well-known π-stacking between aromatic rings, also π-cation interactions between arginines and aromatic rings are known (Flocco and Mowbray,

1994). Additionally, two hydrogen bonds are formed between amines of the purine ring to both the side chain hydroxyl group of T648 and the backbone carbonyl group of D647.

Implications on MAT subdomain dynamics from crystal structures

Variations in the relative positioning of the ferredoxin-like subdomain were reported in previous crystal structures, but a correlation of subdomain mobility to the substrate ambiguity of the domain could not yet be drawn. In chain D of MAT-octanoyl-CoA complex, the MAT domain was found in a unique conformational state. Keeping the α/β-hydrolase part of the domain (backbone atoms (BB) of D488–D611 and D685-D806) as a reference, a superposition was performed with the apo-structure in chain A, the malonyl-bound structure (PDB code 5my0; chain D) and the human KS-MAT (PDB code 3hhd; chain A). The α/β hydrolase domain superimposes very well in all the four models with RMSDs (BB) to the MAT-octanoyl-CoA complex of 0.6 (Chain A), 0.8 (Malonyl-bound chain D), and 0.6 (human chain D) Å, respectively (**Figure 3**A). Largest differences are found in the relative positioning of the ferredoxin-like subdomain with local shifts of up to 7.3 Å between corresponding residues. As also the ferredoxin-like subdomains (BB of 618–674) of all four models themselves superimpose well with RMSDs (BB) between 0.4-0.8 Å, these results clearly illustrate that the ferredoxin-like subdomain describes a rigid-body movement.

When the static X-ray structural information is subjected to a TLS (Translation, Libration and Screw) refinement, the derived anisotropic displacement parameters imply a rotational movement describing the opening

and closing of the active site cleft to allow binding of diverse substrates (Figure S5) (Winn et al., 2001). In order to determine residues contributing most to the positional variability of the ferredoxin-like and the α/β-hydrolase subdomains, we plotted main-chain torsion angles φ and ψ (Ramachandran plot) for the MAT domains of the various structural models. The plot identifies residues A613 and H614 as well as H683 and S684 as undergoing significant changes in main-chain torsion angles (Figure S4). Both sites are the hinges of two subdomain linkers, termed SDL1 (612-617) and SDL2 (675-684), allowing movements of SDL1 and SDL2 of about 7.3 Å and 5.1 Å, respectively (Figure S3A). The positional and conformational variability of the subdomain linkers allows changes in the relative orientation of the subdomains and in the geometry of the active site cleft for the accommodation of chemically and structurally diverse CoA esters (Rittner et al., 2018) (**Figure 3**B).

In addition to the overall dynamics of the MAT fold, the residue R606, responsible for holding the carboxyl group of extender substrates, shows high positional variability in the MAT structural models. The high degree of rotational freedom of the side chain originates likely from the specific property of animal MAT in featuring a phenylalanine at a position (F553, murine MAT numbering), which is otherwise occupied by a conserved glutamine. As shown previously, F553 significantly diminishes the coordination of the R606 side chain by hydrogen-bonding (Rittner et al., 2018). In the octanoyl-bound structure, we could identify a third rotameric state of R606, in addition to the ones found in apo- and malonyl-bound state (Figure S6), which demonstrates that the adaptation of the domain to different substrates is closely connected to the rotational variability of this residue.

Structure of the KS domain in an acylated state

The KS domain forms dimers in type I FAS systems, and contributes the largest area (about 2580 Å^2; see Table S1 for more information) to the overall dimerization interface of animal FAS. The KS domain belongs to the thiolase-superfamily and exhibits the characteristic topology of alternating layers of α-helices and β-sheets (called α/β/α/β/α sandwich motif) (**Figure 4**A). A small vestibule in lateral orientation to the two-fold axis of the condensing part forms the entry to the active site, which is comprised of the active cysteine (C161) as well as two histidine (H293, H331) residues, termed the catalytic triad. The substrate binding tunnel further extends towards the dimer interface, where it merges with the tunnel of the protomer at the two-fold axis (**Figure 4**B).

Overall all the four polypeptide chains of the asymmetric unit align very well onto one another when a KS domain based superposition is performed (RMSDs (BB) of about 0.20-0.25 Å over the residue ranges 1–407 and 824–852) (**Figure 4**C). All four active sites in the KS domains are modified with octanoyl moieties at residue C161. The position and conformation of all active site residues are essentially identical. Only the bound octanoyl chain shows positional variability in the terminal carbon atoms due to an unconstrained rotational freedom of the single bonds. Taking also into account the overall low B-factors observed in the KS part of the crystal structure, this data indicates a relatively low degree of flexibility within the KS domain.

As observed for S581 in the MAT domain, the active cysteine C161 is positioned in a nucleophilic elbow. Here, the positive dipole-moment of the α-helix decreases the pK_a value of the thiol group leading to the increased

nucleophilicity of the sulfur. In a recent computational study, it was reported that the thiol group of the active cysteine is readily deprotonated under physiological condition. This implies a role of H331 in acting as a general acid in catalysis, which is different to acid-base catalysis performed by the active histidine of MAT domains (Lee and Engels, 2014). Such a role of H331 is confirmed by our structural data, as nitrogen (ND1) accepts hydrogen bonds from backbone amides of P332 (3.4–3.6 Å) and E333 (3.0–3.4 Å), whereas the protonated nitrogen (NE2) of H331 is in hydrogen bond distance (3.2–3.4 Å) to the sulfur of the thioester bond at residue C161.

Furthermore, the bound octanoyl chains allow localization of the oxyanion hole, which is created by backbone amides of residues C161 and F395. In all chains, the carbonyl's oxygen of the thioester is in hydrogen bond distance to the corresponding amides of F395 (2.9–3.1 Å) and slightly further apart from backbone amides of C161 (3.1–3.4 Å).

Next, we were interested in conformational changes induced by the loading of an octanoyl chain in comparison to the unbound state. Therefore, the four unbound murine KS domains of the unit cell (PDB code 5my0) were aligned to octanoyl-bound chain A (serving as the representative chain) in a KS domain based superposition (residues 1–407 plus 824–852) (**Figure 4**D). Again, overall RMSDs (BB) were small (0.2-0.3 Å), but the superposition revealed distinct differences in the positions and side chain conformations of some residues. Most prominently, the stretch of residues FGFGG (residues 393-397) is slightly shifted and reorganized upon binding of the octanoyl moiety. This results in the displacement of F395 by 0.8 Å (between corresponding carbon$_\alpha$ atoms) plus the rotation of the side chain by

290 approximately 125°. F395 in the rotamer position of the unbound state
291 clashes with the octanoyl chain in the bound state implying that the
292 rearrangement of F395 is necessary to accommodate substrates.

293 FabB (KAS I) and FabF (KAS II), both elongating β-ketoacyl-ACP
294 synthases of the bacterial type II fatty acid synthesis, have been well-
295 characterized in their three-dimensional structure in an octanoyl-bound state
296 and in a dodecanoyl-bound state, respectively (see e.g. (Olsen et al., 2001;
297 von Wettstein-Knowles et al., 2006; Wang et al., 2006). KS domain based
298 superpositions of FabB and FabF to chain A (BB residues 1–407) show that
299 the active sites display an overall identical architecture implying a conserved
300 catalytic mechanism for the type I KS domain (Figure 5A). An exception is a
301 glutamate residue, which is conserved in CHH class structures (E342 and
302 E349 in FabB and FabF, respectively) and is thought to participate in catalysis
303 by stabilizing a water or cation molecule (Olsen et al., 2001; von Wettstein-
304 Knowles et al., 2006) This acidic residue is exchanged by an alanine in the
305 type I KS domain (A340) excluding an equivalent role in animal FAS.
306
307 ***Specificity of the KS domain for saturated acyl chains***
308 The first step in the KS-mediated Claisen condensation is the
309 transacylation of an acyl-moiety from acyl-ACP to the active site cysteine
310 (**Figure 1**). Considering the similarity of this step to the MAT-mediated
311 transacylation, we aimed at using the continuous fluorometric assay, originally
312 established for transferase analysis (Molnos et al., 2003; Rittner et al., 2018),
313 to investigate the substrate specificity of the KS domain. In doing so, we have
314 constructed KS-MAT^{S581A} for specific KS read-out and the double knockout

315 mutant KS^{C161G}-MAT^{S581A} as a control. All didomain constructs proved to be
316 stable, which was validated by size exclusion chromatography profiles and by
317 melting temperatures obtained in a thermal shift assay (Figure S7). We
318 determined KS-mediated turnover rates from various acyl-CoA esters to a
319 separated, standalone holo-ACP at fixed substrates concentrations
320 (**Figure 5**B). The experiment generally confirmed the results from Witkowski
321 *et al*. of turnover rates increasing with acyl chain-length until maximum rates
322 are reached for octanoyl-CoA and dodecanoyl-CoA (C12-CoA), and
323 decreasing rates with chain-length above C12-CoA (Witkowski et al., 1997).
324 The high value for C12-CoA is not consistent with previous results for the rat
325 homolog and seems to be a specific feature of the heterologously expressed
326 murine KS domain. The specificity of the transfer of acyl-moieties was
327 confirmed with the KS^{C161G}-MAT^{S581A} double knockout mutant (Figure 5B).
328 Further, the substrate specificity of the KS domain was probed with two
329 non-cognate acyl-CoA substrates. While the hydroxybutyryl-CoA, mimicking
330 the intermediate after an initial reduction by the KR-domain, was not accepted
331 as substrate, the non-canonical compound phenylacetyl-CoA was transferred
332 with a reasonable rate. The latter result confirms our previous data that this
333 substrate can also serve as a priming substrate for fatty acid synthesis
334 (Rittner et al., 2019).
335

The KS-mediated transacylation shows kinetic cooperativity

To gain insight into the enzymatic properties of the KS domains, the absolute kinetic parameters for the KS-mediated transacylation from acyl-CoA esters to the ACP domain (as a standalone protein) were determined by the assay described before. The KS-mediated transacylation reaction follows a ping-pong bi-bi mechanism with a covalently bound acyl-enzyme intermediate and can be described with the general equation 1 that is based on standard Michaelis-Menten kinetics (Copeland, 2005). In order to determine absolute kinetic parameters, we have used this equation to globally fit two series of response curves with octanoyl-CoA and myristoyl-CoA at five or six different fixed ACP concentrations (see Methods section). The global fit could only moderately describe the dependence of the apparent turnover rates in respect of the individual ACP concentrations and disclosed systematic deviations in the response curves at low and high substrate concentrations (see Figure S8).

For a better description of the sigmoidal shape of the individual plots, and considering the dimeric nature of the KS domain, we included a Hill coefficient for both substrate concentrations (CoA-Ester and ACP) as described in equation 2. This new fit function clearly delineates both data series without imposing any parameter constraints (see **Figure 6**). The absolute kinetic constants (K') and turnover numbers (k_{cat}) for octanoyl-CoA and myristoyl-CoA are 139 ± 16 µM (K'), 0.09 ± 0.007 s^{-1} (k_{cat}) and 111 ± 8 µM, 0.05 ± 0.002 s^{-1}, respectively. These values lead to specificity constants (k_{cat}/K') in the range of 10^2–10^3 s^{-1} M^{-1}, which indicate rather inefficient priming of the KS domain by CoA-esters. The K'_{ACP} of the

361 standalone ACP was with 16 ± 1.7 µM higher for the transfer of octanoyl
362 moieties than for myristoyl moieties (8 ± 0.8 µM). The calculated Hill
363 coefficients were between 1.7 and 2 for both substrates indicative of a positive
364 cooperativity of the KS domains of a dimeric unit during the transacylation
365 reaction.
366

367 ## Discussion

368 We recently determined kinetic parameters for the murine MAT-
369 mediated transfer of canonical and non-canonical acyl-CoA substrates
370 illustrating the broad substrate tolerance of this domain (Rittner et al., 2018).
371 How can this property be explained, considering high structural conservation
372 to highly specific acyltransferases, like e. g. FabD of *E. coli*? The presented
373 ensemble of MAT structures with non-covalently bound acyl-CoA and
374 covalently bound acyl moieties shines light on this peculiarity. When
375 considering the individual structures as snapshots of an overall
376 conformational variability, data reveals significant dynamics within the MAT
377 domain. Since soaking with octanoyl-CoA trapped the MAT in a very unusual
378 conformation, revealing significant alterations in the position of active site
379 residues, the newly presented structure is particularly informative in this
380 respect. The data shows that substrate polyspecificity of MAT originates from
381 the overall high relative positional dynamics of the α/β-hydrolase and the
382 ferredoxin-like subdomain. A pronounced conformationally variability of the
383 subdomain linkers SDL1 and SDL2, embedded in this large-scale, movement,
384 is further relevant (Figure 3) for the accommodation of the chemically and
385 structurally diverse substrates. Finally, residue R606 modulates substrate

386 polyspecificity by either swinging out to liberate space for the acyl chain (e.g.
387 octanoyl moieties), or by coordinating to the free carboxylic group of extender
388 substrates (e.g. malonyl moieties) (Figure S6). This structural interpretation is
389 supported by enzyme kinetic data as the (wildtype) murine MAT domain
390 shows higher substrate ambiguity as the R606A-mutated MAT domain. In
391 fact, the wildtype MAT domain is even able to accept octanoyl moieties with
392 significantly higher efficiency than the R606A construct (Bunkoczi et al., 2009;
393 Rittner et al., 2018), which could possibly be explained by a smaller number of
394 populated conformational enzyme states (Table 2) (Khersonsky and Tawfik,
395 2010).
396 Can the rather strict KS domain substrate specificity be observed in structural
397 properties? Indeed, the KS domain shows minor structural changes upon
398 binding of an octanoyl chain, resembling a key-and-lock type binding,
399 possessing strict specificities, as also observed for type II systems (von
400 Wettstein-Knowles et al., 2006). The most prominent conformational change
401 upon acylation with saturated acyl chains emerges from the stretch of
402 residues 393-397, in particular residue F395, which is consequently slightly
403 shifted in position and rotated in the side chain by approximately 125°. Its
404 postulated role as a “gatekeeper” seems to be confirmed in animal FAS, as
405 functional groups in the β-position of a bound acyl chain would sterically clash
406 with the phenyl ring (Lee and Engels, 2014; Luckner et al., 2009). In the
407 evolutionarily strongly related protein class of polyketide synthases (PKSs),
408 which share a common KS domain fold, residues at the F395-equivalent
409 position vary, reflecting the key feature of PKSs of condensing β-keto-, β-
410 hydroxy- and α-β-unsaturated acyl substrates (Nguyen et al., 2008).

411 Our setup using a continuous coupled enzyme assay offers a
412 convenient way to investigate the specificity of the KS domain in-depth. The
413 kinetic characterization generally revealed maximum transacylation rates for
414 CoA-esters of medium chain lengths (C8 to C12) and confirmed earlier results
415 of Witkowski *et al.* (Figure 5B) (Witkowski et al., 1997). The unexpected low
416 specific activity for short acyl chains may be attributed to the usage of CoA-
417 esters as donors and substrate concentrations that are insufficient to fully
418 saturate the enzyme. Titration of acyl-CoA substrates at different fixed ACP
419 concentrations for octanoyl- and myristoyl-CoA resulted in sigmoidal individual
420 initial velocity curves (Figure 6). Global fitting of the individual curves was
421 possible when including Hill coefficients for both substrates and the obtained
422 Hill-coefficients of 1.7-2 indicate positive cooperativity. This data can generally
423 be interpreted by an increase in the efficiency of transferring an acyl chain to
424 the active site cysteine of the KS domain, when the other KS of the dimer is
425 already occupied. Such cooperativity of the domains of a KS dimer was
426 postulated for the type II homologs (von Wettstein-Knowles et al., 2006) and
427 could be explained by a conformational interconnection of both active sites
428 that are pointing towards each other and merging at the two-fold axis.

429 Whereas a direct interaction of bound substrates can be ruled out as
430 origin for cooperativity, because the enzyme bound acyl intermediates are too
431 far apart from each other (15.6 Å between terminal C-atoms of octanoyl
432 chains), a stretch of residues (residues 393-397) harboring the gatekeeping
433 F395 and shifting upon acylation may be responsible for this phenomenon.
434 The residues are residing at the dimeric interface and interact with a helix-
435 turn-helix motif of the adjacent protomer (Figure 7A). In the acylated state,

436 side chains of residues M132, Q136 and M139 (adjacent protomer) are
437 slightly altered in their positions due to the rotation of F395, which furthermore
438 leads to a slight shift of the turn (of the helix-turn-helix motif) by up to 0.7 Å
439 (Figure 7B). Structural data reveals a putative coupling of this local
440 rearrangement with active site residues via two hydrogen bonds; one between
441 the side chains of R137 and D158 and the other between the carboxy group
442 of D158 and the backbone amide of A160 (Figure 7C). All three residues are
443 fully conserved in FASs. Based on this structural analysis, cooperativity could
444 hence originate from a subtle reorganization of the active site residues in the
445 neighboring protomer essentially induced by structural changes at the dimer
446 interface occurring during acylation. Further experiments need to elaborate
447 the molecular basis for the observed cooperative behavior of the KS domain
448 as well as to analyze whether cooperativity observed for the transacylation
449 step also extends to the Claisen condensation step.

450 The specific kinetic information about the MAT and KS domains allow
451 us to vividly draw the murine FAS function *in vivo*. The direct loading of the
452 KS domain with acyl-CoA is not relevant *in vivo*, because the specificity
453 constants of the KS-mediated transfer of acyl moieties from acyl-CoAs is
454 more than three orders of magnitude lower than of the respective MAT-
455 mediated transfer (Rittner et al., 2018). Accordingly, substrates are in general
456 loaded at ACP by MAT-mediated transacylation. ACP-bound acetyl- and
457 butyryl moieties are then transferred relatively slowly from the ACP domain to
458 the KS domain and can in a competing pathway escape from FAS by MAT-
459 mediated offloading. Release of short acyl-CoAs via the MAT domain
460 depends on the *in vivo* ratio between malonyl-CoA, acetyl-CoA and free

coenzyme A and hence the availability of an empty MAT's active site. With increasing malonyl-CoA concentrations at higher energetic state of the cell, the offloading event of acetyl- and butyryl moieties gets more and more unlikely and further elongation becomes dominant (Abdinejad et al., 1981). As shown here, once a chain length of six carbons and longer is reached, transacylation from the ACP domain to the KS domain becomes highly efficient until it sharply drops with a chain length of 16 carbons (Figure 5B). According to a key finding of this study, the efficiency of FAS in the elongation of the acyl chain is increased when both reaction chambers are used simultaneously, as acylation of one KS domain of the FAS dimer accelerates the acylation of the other (Figure 6). The substrate specificity of the KS domain is important for the specific production of palmitic acid and is assisted by the substrate specificity of the TE domain for long fatty acyl intermediates (Cheng et al., 2008; Heil et al., 2019; Naggert et al., 1991; Zhang et al., 2011). In summary, FAS produces short acetyl and butyryl-CoA esters in a low energetic state of the cell and almost exclusively palmitic acid (C16) at high energetic states.

The presented structural and mechanistic study deepens our molecular understanding of the two initial catalytic domains in animal fatty acid synthesis. Such detailed information is particularly interesting as FAS got into focus as a target for combinatorial anti-cancer therapy. Especially, the plasticity of the MAT domain shall be highlighted, allowing to accommodate a broad range of chemically diverse compounds. This may aid future rational drug discovery campaigns and enlarge the pool of potentially screened lead structures.

Acknowledgments

This work was supported by a Lichtenberg grant of the Volkswagen Foundation to M.G. (grant number 85701). Further support was received from the LOEWE program (Landes-Offensive zur Entwicklung wissenschaftlich-ökonomischer Exzellenz) of the state of Hesse conducted within the framework of the MegaSyn Research Cluster.

Authors contribution

A.R. performed protein expression, purification experiments, enzymatic assays and analyzed corresponding data. A.R. conceived the project. M.G. designed the research. A.H. performed kinetic experiments with the KS domain using octanoyl-CoA under supervision of A.R. Crystallization was performed by A.R., A.H. and K.S.P. Crystal structure was solved by K.S.P. A.R., K.S.P. and M.G. analyzed data and wrote the manuscript.

Declaration of interests

The authors declare no competing interests.

Figure Legends

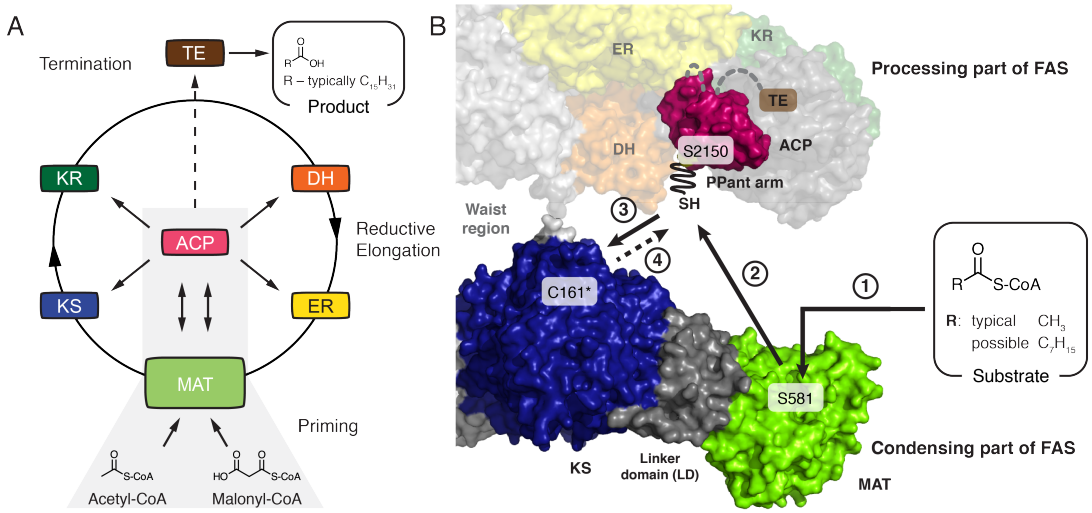

Figure 1: Priming of animal fatty acid synthesis. In a first step, the substrate is selected by the MAT domain and transferred to the ACP domain (2. step) from where it is passed on to the KS domain (3. step). Important active site residues are highlighted and C161 is marked with an asterisk. Crystal structure of porcine FAS (PDB code 2vz9) and NMR structure of rat ACP (PDB code 2png) are depicted in surface representation (Maier et al., 2008; Ploskoń et al., 2008). Domains of one protomer of FAS homodimer are colored. Domain nomenclature: MAT, malonyl-/acetyltransferase; ACP, acyl carrier protein; KS, ketosynthase; KR, ketoreductase; DH, dehydratase; ER, enoylreductase; TE, thioesterase; PPant arm expand fully in the figure.

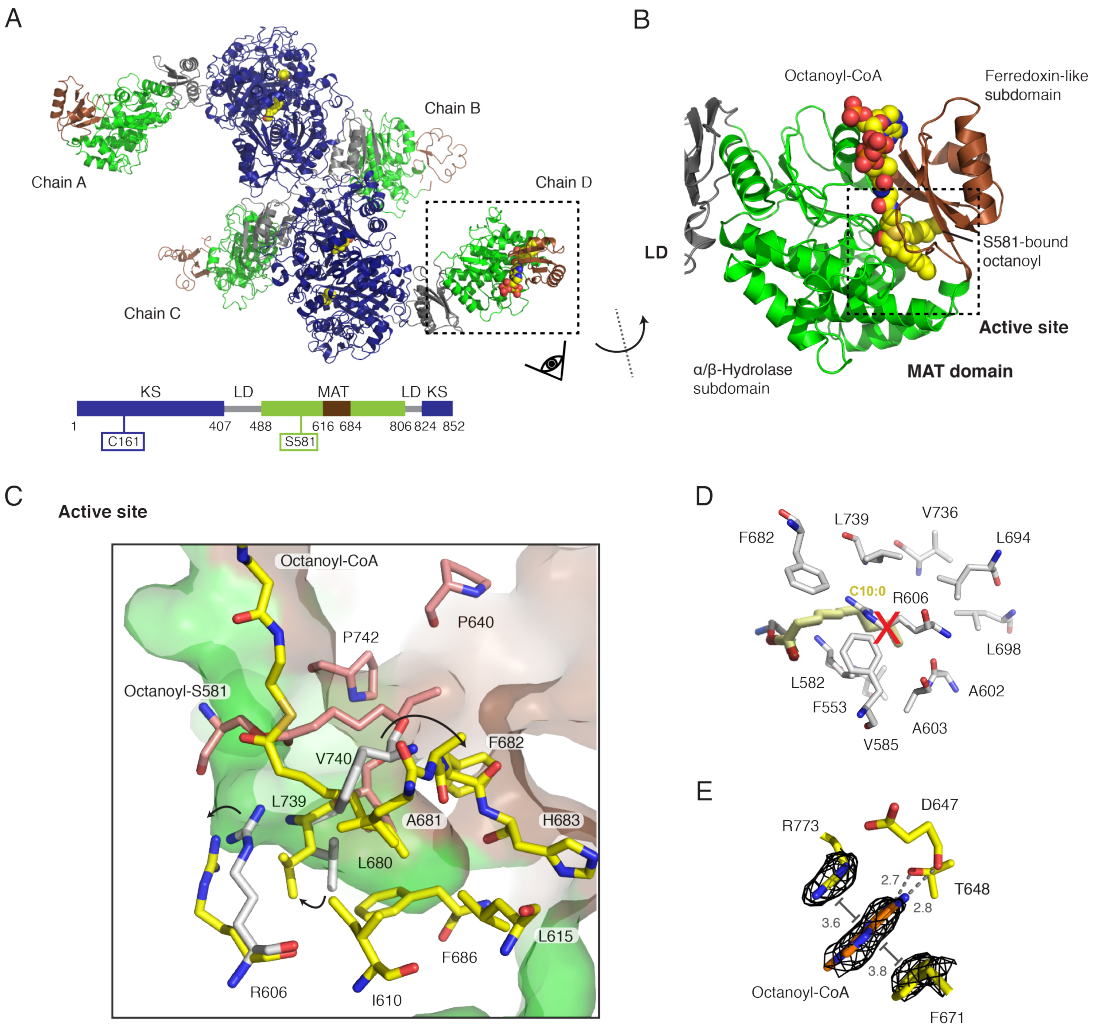

Figure 2: Octanoyl-loaded MAT domain. (A) Polypeptide chains in the unit cell with bound octanoyl moieties in yellow in sphere representation. Domains and folds are coloured as depicted in the attached cartoon. (B) Zoom into the MAT domain in chain D. The active site is embedded in a cleft between the α/β-hydrolase (green) and the ferredoxin-like (brown) subdomains. The active site serine (S581) was found in an octanoyl-bound state with an additional octanoyl-CoA molecule non-covalently attached to the active site tunnel (see Figure S2 for FEM (Afonine et al., 2015) and Polder maps (Liebschner et al., 2017)). (C) Zoom into the MAT active site. Residues interacting with the serine-bound octanoyl chain and the octanoyl CoA are coloured in red and yellow, respectively. Movements of select residues upon binding of an

531 octanoyl moiety in comparison with the human MAT structure (grey) are
532 indicated by arrows. (D) Orientation of a decanoyl chain as reported by
533 Bunkoczi *et al.*.(Bunkoczi et al., 2009). Atomic coordinated originate from
534 decanoyl chain computationally modelled into the human MAT variant R606A
535 (pdb code: 2jfd). Postulated interacting residues of the human MAT domain
536 are shown in grey. (E) Binding site of the nucleobase of the CoA moiety at the
537 MAT surface. The adenine is coordinated via hydrogen bonding by with
538 residues D647 and T648 and via π-stacking and π-cation interactions with
539 residues F671 and R773 were identified.
540

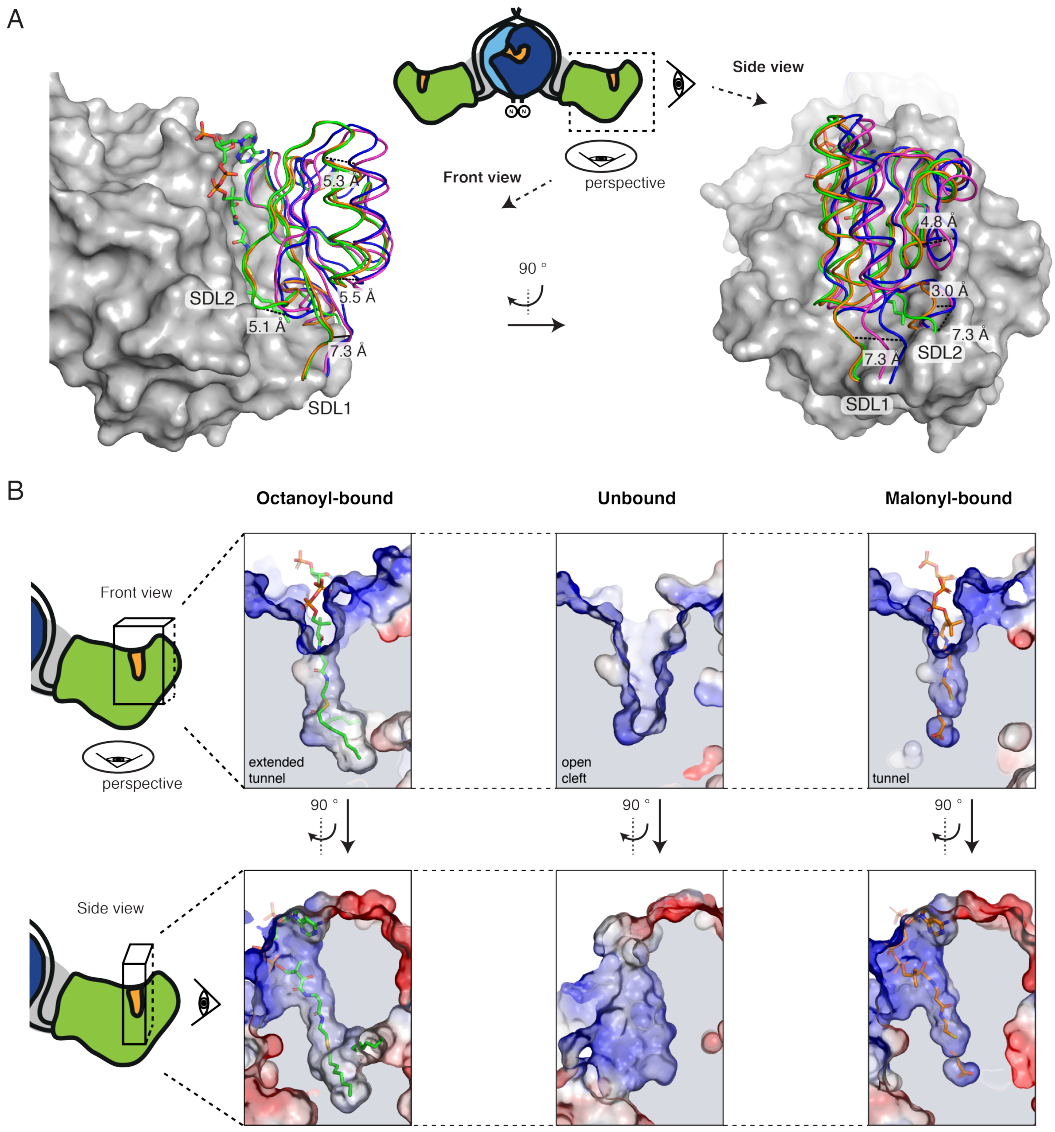

Figure 3: Conformational variability of the MAT active site. (A) α/β-Hydrolase fold centrered superposition (BB of residues 488–613 and 685-806) of four MAT domains in different acyl-bound states. Chain A (blue) and chain D (green) from the octanoyl-CoA soaked crystal (PDB code 6rop), malonyl-bound (orange) (PDB code 5my0; chain D) and apo human MAT (purple) (PDB code 3hhd; chain A) were used. The α/β-hydrolase subdomain is shown in surface depiction and the ferredoxin-like fold in cartoon loops. Selected distances between corresponding residues indicate the mobility of the subdomains with a relative movement of the ferredoxin-like fold of up to

551 7.3 Å. (B) Different active site and entry tunnel shapes upon substrate
552 binding. Surface depictions of active sites of chain D (left panel) and A
553 (middle) from the octanoyl-bound structure and chain D (right panel) from the
554 malonyl-bound structure are shown in two perspectives. Surfaces are shown
555 in surface electrostatic representation calculated with PyMOL and shown in
556 default coloring with positive potential depicted in blue and negative potential
557 in red. Views as in (A).
558

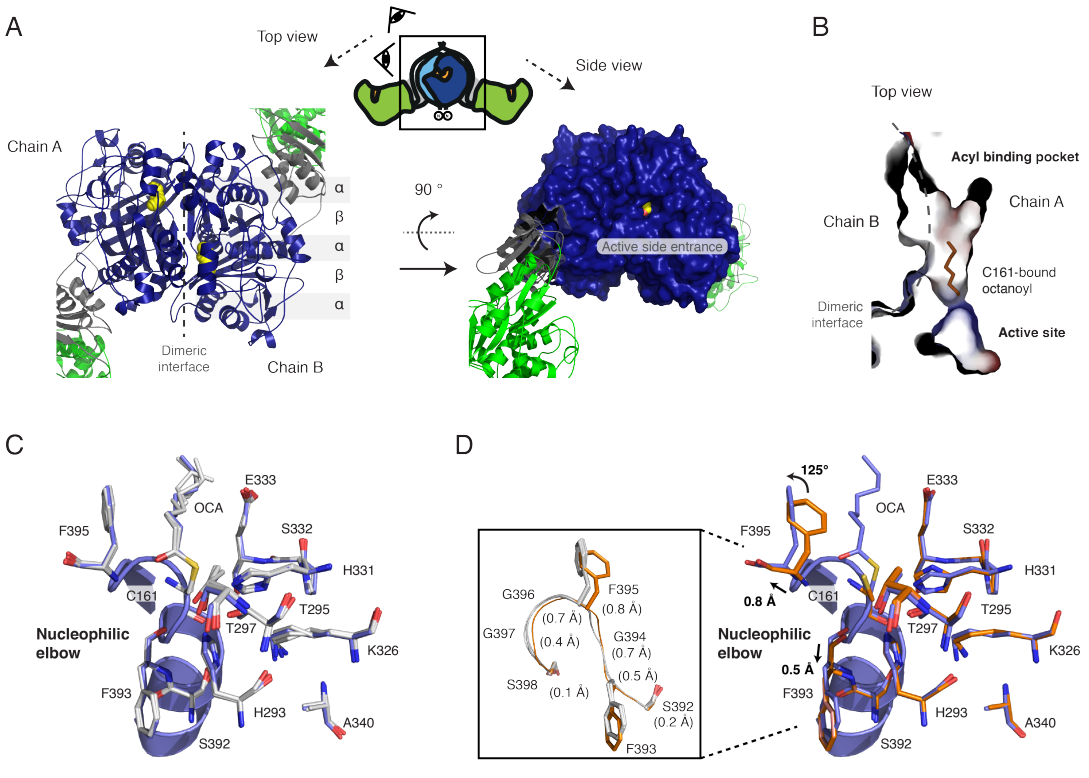

559

560 **Figure 4: Octanoyl loaded KS domain.** (A) Top view on the dimeric KS
561 domain in cartoon depiction showing the topology of the α/β/α/β/α sandwich
562 motif (left panel). A surface depiction of the KS domain in side view highlights
563 the active site entrance. Color codes as in Figure 2A is used with the bound
564 octanoyl chain shown in yellow in sphere representation (right panel). (B)
565 Active site and acyl binding cavity of the KS domain. In addition to the
566 substrate binding cavity between the dimer interface, a small side chamber is
567 visible in the monomer. The binding cavity is shown with surfaces colored in
568 electrostatic potential (colored as in Figure 3). (C) Active site of KS showing
569 important residues for catalysis, reported for homologous KAS I (FabB)
570 (Olsen et al., 2001). Three chains (B-D) with bound octanoyl moieties were
571 aligned to chain A (blue) by a KS based superposition (BB of residues 1–407
572 and 824–852). All residues adopt essentially the same conformation with
573 some variability in the terminal carbon atoms of the octanoyl chain. (D) A

574 similar KS based superposition was performed with the four apo-KS domains
575 (orange; PDB code 5my0) and the octanoyl-bound chain A (blue). Upon
576 octanoyl binding, the individual residues of the stretch 393-397 are shifted by
577 0.4-0.8 Å (highlighted in the inlet). Furthermore, the side chain of F395 is
578 rotated by approximately 125°.
579

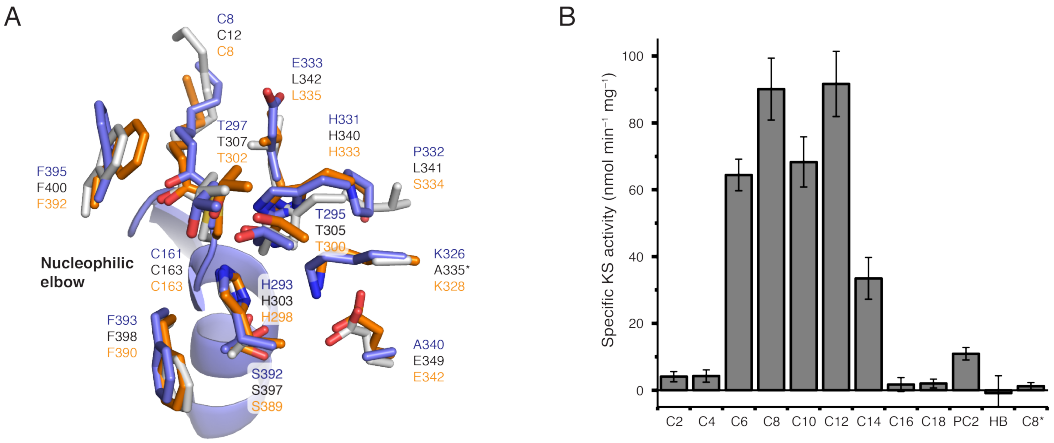

580

581 **Figure 5: Chain-length specificity of KS and comparison of the KS**
582 **domain with FabB and FabF from *E.* coli.** (A) Comparison of important
583 active site residues of the murine type I KS domain (chain A; blue) with FabB
584 (orange; PDB code 2bui) and FabF (grey; PDB code 2gfy) from *E. coli* (von
585 Wettstein-Knowles et al., 2006; Wang et al., 2006). All three proteins were
586 solved in the acyl bound state and *E. coli* proteins were aligned to chain A
587 (blue) by a KS based superposition (BB of residues 1–407). The asterisk
588 indicates that a variant of FabF was crystalized possessing a K335A mutation.
589 (B) Chain-length specific KS-mediated transacylation activity. The specific KS-
590 mediated activity was determined at fixed substrate (500 µM) and holo-ACP
591 (75 µM) concentrations using the αKGDH-assay. The asterisk indicates usage
592 of variant $KS^{C161G}MAT^{S581A}$ as negative control. Abbreviations refer to acyl-
593 CoA esters with different chain lengths and PC2 and HB refer to phenylacetyl-
594 CoA and hydroxybutyryl-CoA, respectively.

595

596

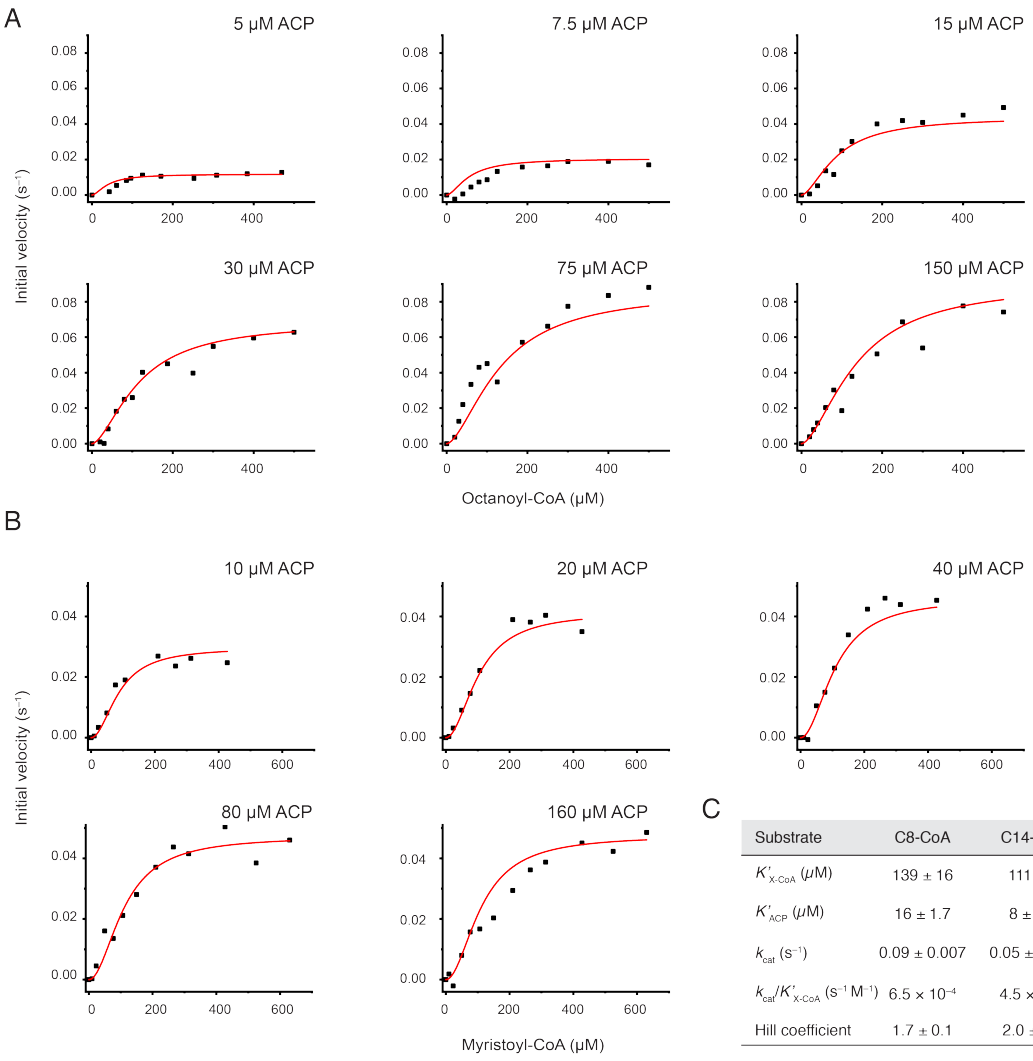

C

Substrate	C8-CoA	C14-CoA
$K'_{X\text{-}CoA}$ (μM)	139 ± 16	111 ± 8
K'_{ACP} (μM)	16 ± 1.7	8 ± 0.8
k_{cat} (s^{-1})	0.09 ± 0.007	0.05 ± 0.002
$k_{cat}/K'_{X\text{-}CoA}$ ($s^{-1}\,M^{-1}$)	6.5×10^{-4}	4.5×10^{-4}
Hill coefficient	1.7 ± 0.1	2.0 ± 0.2

Figure 6: Comprehensive analysis of the KS-mediated transfer of octanoyl and myristoyl moieties. (A) Initial velocities plotted against octanoyl-CoA (C8-CoA) concentrations at six fixed ACP concentrations. (B) Initial velocities plotted against myristoyl-CoA (C14-CoA) concentrations at five fixed ACP concentrations. All data series were fit globally with the Hill equation due to the sigmoidal shape. (C) Absolute kinetic parameter derived from the respective global fits for octanoyl-CoA (C8-CoA) and myristoyl-CoA (C14-CoA), respectively. No parameters constraints were imposed during curve fitting. The constant *K*' of the Hill equation is related to the Michaelis constant K_m, but also contains terms related to the effect of substrate

608 occupancy at one site on the substrate affinity of the other site.

609

610

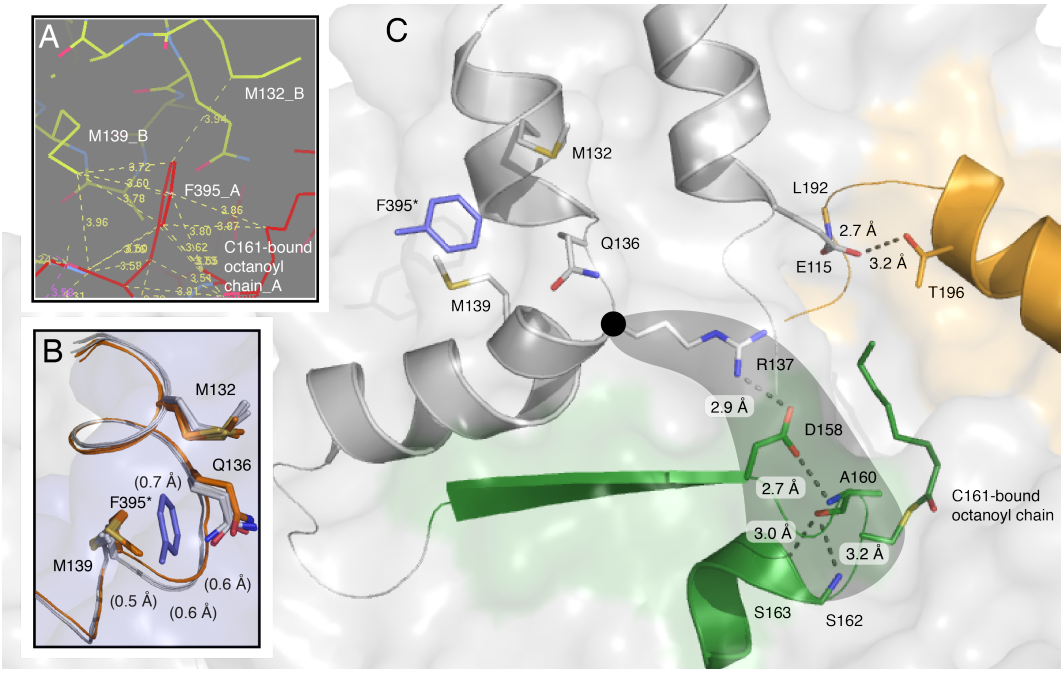

611

612 **Figure 7: Structural interconnection of both KS active sites of a dimer.**
613 (A) Identification of M132 and M139 as F395-interacting residues in the other
614 chain of the dimer. Chain A and chain B are colored in red and yellow,
615 respectively. Analysis was performed with the software Coot. (B) Different
616 side-chain conformations of M132, Q136 and M139 and subtle backbone shift
617 between unbound (orange) and octanoyl-bound (grey) KS active sites. All four
618 chains of both crystal structures (5my0 and 6rop) were aligned by a KS based
619 superposition (BB of residues 1–407). F395 (blue) is depicted for clarity and
620 the asterisks indicates the hypothetical position of the residue in the
621 respective other protomer. (C) Hydrogen bonding between R137, D158 and
622 the nucleophilic elbow (green) including the active site residue C161.

623

624 **Table 1. Data collection and refinement statistics**

	Wild-type soaked with octanoyl-CoA
Data Collection	
Space group	$C222_1$
Cell dimensions	
a, b, c (Å)	147.4 354.0 218.5
α, β, γ (°)	90 90 90
Resolution (Å)	50-2.7 (2.75 – 2.7)
No. of reflections	2195612(110844)
R_{meas}	0.16(2.4)
I/σI	13.9(1.4)
$CC_{1/2}$	0.99(0.62)
Completeness (%)	98.2(98.8)
Redundancy	14.3(14.5)
Refinement	
R_{work}/R_{free} (%)	18.4(23.2)
No. of unique reflections	145548
Average *B* factors (Å^2)	

Protein	78.9
Wilson *B* factor	58.4
RMSD from ideality	
Bond length (Å)	0.007
Bond angles (°)	1.5
Ramachandran statistics	
Favored regions (%)	93.43
Allowed regions (%)	5.05
Outliers (%)	1.52

Highest resolution shell is shown in paranthenses.

Table 2. Kinetic analysis of the transacylation reaction with octanoyl-CoA at a fixed acceptor concentration of 60 µM ACP (n = 4)

Substrate	K_m^{app} (µM)			k_{cat}^{app} (s^{-1})			k_{cat}/K_m (M^{-1} s^{-1})					Hydrolysis rate 10^{-3} (s^{-1})		
Wildtype*	0.7	±	0.3	4.1	±	0.3	5.6	±	2.2	×	10^6	6.1	±	1.0
R606A variant	4.9	±	0.7	0.037	±	0.008	7.6	±	2.0	×	10^3	2.3	±	3.4

*Previously published (Rittner et al., 2018).

STAR Methods

Key Resources Table

REAGENT or RESOURCE	SOURCE	IDENTIFIER
Chemicals, Peptides, and Recombinant Proteins		
D-Desthiobiotin	IBA Lifesciences	Cat#2-1000-002
CoA-esters	Merck	
αKGDH (porcine heart)	Merck	Cat#K1502
Thiamine pyrophosphate chloride (TPP)	Merck	Cat#C8754
α-Ketoglutaric acid	Merck	Cat#K1750
β-Nicotinamide adenine dinucleotide hydrate (NAD^+)	Merck	Cat#N7004
Deposited Data		
Atomic coordinates, octanoyl-bound murine KS-MAT structure	Protein Data Bank	PDB: 6rop
Experimental Models: Organisms/Strains		
E. coli Stellar™ Competent Cells	Clontech	Cat# 636766
E. coli BL21 Gold (DE3) Cells	Agilent	Cat#230132
Recombinant DNA		
pAR69_StrepI_m(KS_MAT)_H8_pET22b	Addgene	Cat#122849
pAR70_StrepI_m(KS(C161G)_MAT)_H8_pET22b	(Rittner et al., 2018)	N/A
pAR71_StrepI_m(KS(C161G)_ATmut(R(606A))_H8_pET22b	(Rittner et al., 2018)	N/A
pAR159_StrepI_m(KS_MAT(S581A))_H8_pET22b	This Study	N/A
pAR160_StrepI_m(KS(C161G)_MAT(S581A))_H8_pET22b	This Study	N/A
pAR352_StrepII_mACP_H8_RBS_SFP_pET22b	(Rittner et al., 2018)	N/A
Sequence-Based Reagents		

AR310_mMAT_S581A_for: 5'-ggcatcattgggcacGccttgggagaggttgcctgtgg-3'	Merck	N/A
AR301_mMAT_S581X_rev: 5'-gtgcccaatgatgccgtcag-3'	Merck	N/A
Software and Algorithms		
COOT	Emsley and Cowtan, 2004	N/A
PyMOL 2.4	Schrodinger, LLC	N/A
OriginPro 8.5	OriginLab, USA	N/A
CFX Maestro 1.0	BIO-RAD	N/A

Contact for Reagent and Resource Sharing

Further information and requests for reagents may be directed to, and will be fulfilled by the corresponding author Martin Grininger (grininger@chemie.uni-frankfurt.de).

Experimental Model and Subject Details

Method Details

Reagents and Constructs

All CoA-esters, β-NAD^+, NADH, α-ketoglutarate dehydrogenase (porcine heart) (αKGDH), α-ketoglutaric acid, thiamine pyrophosphate (TPP), and EDTA were purchased from Merck. BSA was from Serva. Restriction

647 enzymes were bought from NEB biolabs. IPTG was from Carl Roth. Ni-NTA
648 affinity resin was from Qiagen and 5 mL Strep-Tactin® columns were
649 purchased from IBA technologies. Purity of CoA-esters was confirmed by
650 HPLC-UV analysis before usage.

651 Point mutations were introduced by PCR based cloning. Fragments for
652 pAR159 and pAR160 were generated by amplification of pAR69 (Addgene,
653 #122849) and pAR70 (Rittner et al., 2018) with the primer pair: AR301 (5'-
654 gtgcccaatgatgccgtcag-3') and AR310 (5'-ggcatcattgggcacGccttgggagaggttgc
655 ctgtgg-3'). PCR products were treated with Dpn1 (NEB), purified by gel
656 electrophoresis and DNA was extracted with the Wizard® SV Gel and PCR
657 Clean-Up System (Promega). Purified DNA was transformed into *E. coli*
658 Stellar™ Competent Cells, 5 mL LB cultures were grown and plasmids were
659 isolated with the PureYield™ Plasmid Miniprep System (Promega).
660 Sequences of all plasmids were confirmed with the "dye terminator" method.
661

662 ***Expression and purification of KS-MAT variants***

663 All plasmids were transformed into chemically competent *E. coli* BL21
664 Gold (DE3) cells. The transformants were grown overnight at 37 °C in 20 mL
665 LB (100 µg mL^{-1} ampicillin (amp) and 1 % (w/v) glucose) medium. Pre-
666 cultures were used to inoculate 1 L TB medium (100 µg mL^{-1} amp). Cultures
667 were grown at 37 °C until they reached an optical density (OD_{600}) of 0.5–0.6.
668 After cooling at 4 °C for 20 min, cultures were induced with 0.25 mM IPTG,
669 and grown for additional 16 h at 20 °C and 180 rpm. Cells were harvested by
670 centrifugation (4,000 rcf for 20 min). The cell pellets were resuspended in lysis
671 buffer (50 mM potassium phosphate, 200 mM potassium chloride, 10 % (v/v)

672 glycerol, 1 mM EDTA, 30 mM imidazole (pH 7.0)) and lysed by French press.
673 After centrifugation at 50,000 rcf for 30 min, the supernatant was mixed with
674 1 M $MgCl_2$ to a final concentration of 2 mM. The cytosol was transferred to Ni-
675 NTA-columns and washed with 5 column volumes (CV) wash buffer (lysis
676 buffer without EDTA). Bound protein was eluted with 2.5 CV elution buffer
677 (50 mM potassium phosphate, 200 mM potassium chloride, 10 % (v/v)
678 glycerol, 300 mM imidazole (pH 7.0). The eluent was transferred to Strep-
679 Tactin-columns, and washed with 5 CV strep-wash buffer (250 mM potassium
680 phosphate, 10 % (v/v) glycerol, 1 mM EDTA, (pH 7.0)). Proteins were eluted
681 with 2.5 CV elution buffer (strep-wash buffer containing 2.5 mM D-
682 desthiobiotin). After concentration to 10–20 mg mL^{-1}, the proteins were frozen
683 in liquid nitrogen and stored at –80 °C. Samples were thawn at 37 °C for
684 30 min and further polished by size-exclusion chromatography (SEC) using a
685 Superdex 200 GL10/300 column equilibrated with the strep-wash buffer.
686 Proteins were concentrated again to 10–20 mg mL^{-1} and stored frozen in
687 aliquots using liquid nitrogen.
688
689 ***Expression and purification of ACP***
690 ACP for the activity assay was produced by co-expression with the 4'-
691 phosphopantetheinyl transferase Sfp from the bicistronically organized vector
692 pAR352 (Rittner et al., 2018).The plasmid was transformed into chemically
693 competent *E. coli* BL21 Gold (DE3) cells. Overnight cultures were grown in
694 40 mL LB (100 µg mL^{-1} ampicillin (amp) and 1 % (w/v) glucose) at 37 °C. 2 L
695 TB medium (100 µg mL^{-1} amp) was inoculated with the overnight culture and
696 incubated at 37 °C until an optical cell density (OD_{600}) of 0.5–0.6 was

reached. After cooling at 4 °C for 20 min, cultures were induced with 0.25 mM IPTG, and grown for additional 16 h at 20 °C and 180 rpm. Cells were harvested by centrifugation, resuspended in lysis buffer and lysed by French press. After centrifugation (50,000 rcf for 30 min), the supernatant (supplemented with 2 mM $MgCl_2$) was transferred to Ni-NTA-columns and washed with 5 CV wash buffer. The protein was eluted with elution buffer (wash buffer containing 300 mM imidazole) and concentrated. Pooled fractions, were separated on a Superdex 200 HiLoad 16/60 or 26/60 SEC column equilibrated with buffer (50 mM potassium phosphate, 200 mM potassium chloride, 10 % (v/v) glycerol, 1 mM EDTA). All fractions containing monomeric ACP were pooled and concentrated to 10-20 mg mL^{-1}.

Protein concentration

Protein concentrations were calculated from the absorbance at 280 nm, which was recorded on a NanoDrop 2000c (Thermo scientific). Extinction coefficients were calculated from the primary sequence without *N*-formylmethionine with CLC Main workbench (Qiagen). Absorbance 1 g L^{-1} at 280 nm (10 mm): 1.053 for KS-MAT and 0.475 for ACP.

Crystallization, data collection and structure determination

Crystallization conditions for KS-MAT were as previously published (Rittner et al., 2018). Single-crystals were obtained at 0.2 M potassium-sodium tartrate, 25 % (w/v) PEG 3350 at 20 °C to sizes of about 75 × 75 × 75 μm^3. Drops with the crystals were supplemented with 0.5 µl of 10 mM octanoyl-CoA (Merck) for up to 2 minutes and subsequently treated

722 with a cryosolution containing 20 % (v/v) glycerol in the mother liquor. The
723 crystal was then picked in a nylon fiber loop and vitrified into liquid nitrogen.
724 Single wavelength X-radiation diffraction dataset was collected at the Swiss
725 Light Source (X06SA), and maintained at 100 K, while data were recorded
726 onto a detector (DECTRIS EIGER 16M). Using the 'goeiger.com' pipeline at
727 X06SA, data reduction was performed within *XDS* (Kabsch, 2010), for
728 indexing and integration, and *Aimless* (Evans, 2005) for scaling. The
729 structural model of a monomer from the murine FAS KS-MAT didomain
730 complexed with Malonyl-CoA (pdb accession code 5my0) was used to solve
731 the phase problem using the program *Molrep* (Vagin and Teplyakov, 1997).
732 After an initial rigid-body refinement, the model was subjected to repeated
733 cycles of restrained refinement with *REFMAC*5 (Murshudov et al., 2011) with
734 manual model building using *Coot* (Emsley et al., 2010). Data collection and
735 refinement statistics are given in Table 1. Electron density maps were
736 generated by Phenix (Afonine et al., 2012).
737
738

Thermal shift assay

Thermal shift assays were performed as previously reported (Rittner et al., 2019). Briefly, 2 µL of protein solution (20 µM) were mixed with 21 µL of the respective buffer and 2 µL of SYPRO Orange protein gel stain (5000 × diluted), then fluorescence was measured from 5 °C to 95 °C with a step of 0.5 °C min^{-1}, with excitation wavelength set to 450-490 nm, and emission wavelength to 560-580 nm. Data was analyzed with the software CFX Maestro 1.0.

α-Ketoglutarate dehydrogenase coupled activity assay

The enzyme-coupled assay was performed as previously published (Rittner et al., 2018), which was adapted from reference (Molnos et al., 2003). Assays (octanoyl-CoA transacylation of the KS^{C161G}-MAT^{R606A} variant and the series of response curves for the KS-mediated transacylation of octanoyl moieties) were run in 96-well f-bottom microtiter plates (Greiner Bio-one) and NADH fluorescence was monitored using a ClarioStar microplate reader equipped with a dispenser (BMG labtech) at the following settings; excitation: 348-20 nm; emission: 476-20 nm; gain: 1900; focal height: 5.2 mm; flashes: 70; orbital averaging: 4 mm.

Within this study we reduced the assay volume first to 50 µL in 96-well Half Area Microplates (Greiner Bio-one) and then to 20 µL in 384-well Small Volume HiBase Microplates (Greiner Bio-one) for practical and financial reasons. The chain-length specificity of the KS domain (Figure 5) and the series of response curves for the KS-mediated transacylation of myristoyl moieties (Figure 6B) were measured in half-area plates and 384-well plates,

764 respectively. New calibration curves with NADH and control measurements
765 were performed for both smaller plate formats. Settings for the microplate
766 reader were for half-area plates: 348-20 nm; emission: 476-20 nm; gain:
767 1500; focal height: 5.6 mm; flashes: 17; orbital averaging: 1 mm; and for 384-
768 well plates: 348-20 nm; emission: 476-20 nm; gain: 1500; focal height:
769 11.9 mm; flashes: 17; orbital averaging: off.

770 Same procedures were used in preparation of assays even if they had
771 different volumes. Briefly, four different solutions were prepared in assay
772 buffer (50 mM sodium phosphate, 10 % (v/v) glycerol, 1 mM DTT, 1 mM
773 EDTA (pH 7.6), filtered and degased). Solution 1 (Sol 1) contained murine
774 KS-MAT in a 3.33-fold or 4-fold concentrated stock solution and
775 supplemented with 0.1 mg mL^{-1} BSA. Solution 2 (Sol 2) contained 8 mM α-
776 ketoglutaric acid, 1.6 mM NAD^+, 1.6 mM TPP and 60 mU/100 µL αKGDH,
777 representing a 4-fold concentrated stock. Solution 3 (Sol 3) contained 4-fold
778 concentrated CoA-esters, typically between 0.4–2800 µM. Solution 4 (Sol 4)
779 finally contained 5-fold or 4-fold concentrated murine ACP, typically between
780 20-800 µM. The components were pipetted in order: 30 µL Sol 1 (3.33-fold),
781 25 µL Sol 2 and 25 µL Sol 3 for 96-well plates; 15 µL Sol 1 (3.33-fold),
782 12.5 µL Sol 2 and 12.5 µL Sol 3 for 96-well half-area plates and 5 µL Sol 1 (4-
783 fold), 5 µL Sol 2 and 5 µL Sol 3 for 384-well plates, followed by mixing. The
784 transfer reaction was initiated by 20 µL and 10 µL Sol 4 (5-fold)) or 5 µL Sol 4
785 (4-fold), which was added by the dispenser. The final concentrations of all
786 ingredients were 50 mM sodium phosphate, pH 7.6, 10 % (v/v) glycerol, 1 mM
787 DTT, 1 mM EDTA, 2 mM α-ketoglutaric acid, 0.4 mM NAD^+, 0.4 mM TPP,
788 15 mU/100 µL αKGDH, 0.03 mg mL^{-1} BSA, 100-200 nM KS-MAT, 5–160 µM

789 ACP, 0.1–700 µM X-CoA (where X refers to the respective acyl-moiety of the
790 assay). The background noise of the assay set-up was determined with assay
791 buffer supplemented with 0.1 mg mL^{-1} BSA. Equidistant kinetic
792 measurements were taken every 5-22 s for ca. 5 min at 30 °C.
793
794 ***Transacylation kinetics of the MAT^{R606A} variant for octanoyl moieties***
795 Determining the apparent Michaelis-Menten constant is an iterative
796 process. Pre-experiments were initially performed to approach the
797 approximate value of K_m. Final concentrations of enzyme and ACP were
798 100 nM and 60 µM, respectively. Eight data points were collected that cover
799 substrate concentrations (Sol 3) of 0.2 × K_m; 0.3 × K_m; 0.5 × K_m; 0.75 × K_m;
800 1.25 × K_m; 2 × K_m; 3 × K_m; 5 × K_m. Every measurement was performed in
801 technical triplicates and the corresponding background signal was
802 substracted. Experiments were setup in a way such that changes in signal
803 remained linear during the time ranges of measurement. Data were collected
804 in biological replicates (n = 4) and were fit with the Michaelis-Menten function
805 using OriginPro 8.5 (OriginLab, USA).
806
807 ***Chain-length specificity of the KS domain***
808 KS-mediated transacylation of acyl-CoAs were measured at fixed
809 enzyme (200 nM), ACP (75 µM) and acyl-CoA (500 µM) concentrations.
810 Turnover rates were determined by linear fit and error bars reflect the
811 standard deviation from three biological replicates (n = 3).
812
813

814 ***Analysis of KS-mediated transfer of octanoyl and myristoyl moieties***

815 Initial velocities were determined for twelve different CoA-ester
816 concentrations at six (octanoyl-CoA) and five (myristoyl-CoA) fixed ACP
817 concentrations. Enzyme concentration was 200 nM. Every measurement was
818 performed in one biological replicate (n = 1) and the corresponding
819 background signal was subtracted. Both series of response curves were
820 globally fit using all data without any parameter constraints. The global fit was
821 performed with OriginPro 8.5 (OriginLab, USA) using the following equations
822 for the ping-pong mechanism:

823

$$v = \frac{k_{cat}[\mathrm{AT_0}][XCoA][ACP]}{[XCoA]K_m^{ACP} + [ACP]K_m^{XCoA} + [XCoA][ACP]} \quad [1]$$

824 Hill-type variation:

$$v = \frac{k_{cat}[\mathrm{AT_0}][XCoA]^h[ACP]^h}{[XCoA]^hK'_{ACP} + [ACP]^hK'_{XCoA} + [XCoA]^h[ACP]^h} \quad [2]$$

825

826 **Quantification and Statistical Analysis**

827 Statistical parameters are reported in Figure Legends and in Method
828 Details. Biological replicates refer to independently expressed and purified
829 enzymes. Transacylation kinetics of the MAT^{R606A} variant for octanoyl
830 moieties was performed in four biological replicates, with error bars indicating
831 SD. Chain-length specificity of the KS domain was performed in three
832 biological replicates, with error bars indicating SD. Both series of response

833 curves were performed in one biological replicate and the errors are standard
834 errors from the global fit.
835

836 Data and Software Availability

837 Accession numbers for the atomic coordinates for the octanoyl-bound murine
838 KS-MAT structure reported in this paper is PDB: 6rop. X-ray diffraction data
839 are publicly available at https://zenodo.org/deposit/2785017.
840

841 Supplementary Material

842 Additional supporting information may be found in the online version of this
843 article.

844 References

845 Abdinejad, A., Fisher, A.M., and Kumar, S. (1981). Production and Utilization
846 of Butyryl-CoA by Fatty Acid Synthetase from Mammalian Tissues. Arch.
847 Biochem. Biophys. *208*, 135-145.

848 Afonine, P.V., Grosse-Kunstleve, R.W., Echols, N., Headd, J.J., Moriarty,
849 N.W., Mustyakimov, M., Terwilliger, T.C., Urzhumtsev, A., Zwart, P.H., and
850 Adams, P.D. (2012). Towards automated crystallographic structure refinement
851 with phenix.refine. Acta Cryst (2012). D68, 352-367
852 [doi:10.1107/S0907444912001308], 1-16.

853 Afonine, P.V., Moriarty, N.W., Mustyakimov, M., Sobolev, O.V., Terwilliger,
854 T.C., Turk, D., Urzhumtsev, A., and Adams, P.D. (2015). FEM: feature-
855 enhanced map. Acta Crystallogr. D Biol. Crystallogr. *71*, 646-666.

856 Beld, J., Lee, D.J., and Burkart, M.D. (2015). Fatty acid biosynthesis revisited:
857 structure elucidation and metabolic engineering. Mol. Biosyst. *11*, 38-59.

858 Boehringer, D., Ban, N., and Leibundgut, M. (2013). 7.5-Å Cryo-EM Structure
859 of the Mycobacterial Fatty Acid Synthase. J. Mol. Biol., 1-9.

860 Buckley, D., Duke, G., Heuer, T.S., O'Farrell, M., Wagman, A.S., McCulloch,
861 W., and Kemble, G. (2017). Fatty acid synthase - Modern tumor cell biology
862 insights into a classical oncology target. Pharmacol. Ther. *177*, 23-31.

Buckner, J.S., Kolattukudy, P.E., and Rogers, L. (1978). Synthesis of Multimethyl-Branched Fatty Acids by Avian and Mammalian Fatty Acid Synthetase and Its Regulation by Malonyl-CoA Decarboxylase in the Uropygial Gland. Arch. Biochem. Biophys. *186*, 152-163.

Bunkoczi, G., Misquitta, S., Wu, X., Lee, W.H., Rojkova, A., Kochan, G., Kavanagh, K.L., Oppermann, U., and Smith, S. (2009). Structural Basis for Different Specificities of Acyltransferases Associated with the Human Cytosolic and Mitochondrial Fatty Acid Synthases. Chem. Biol. *16*, 667-675.

Chen, A., Re, R.N., and Burkart, M.D. (2018). Type II fatty acid and polyketide synthases: deciphering protein–protein and protein–substrate interactions. Nat. Prod. Rep. *35*, 1029-1045.

Cheng, F., Wang, Q., Chen, M., Quiocho, F.A., and Ma, J. (2008). Molecular docking study of the interactions between the thioesterase domain of human fatty acid synthase and its ligands. Proteins: Structure, Function, and Bioinformatics *70*, 1228-1234.

Copeland, R.A. (2005). Enzymes - A Practical Introduction to Structure, Mechanism and Data Analysis - 2nd Edition (Weinheim, Germany: Wiley-VCH Verlag GmbH).

Dean, E.J., Falchook, G.S., Patel, M.R., Brenner, A.J., Infante, J.R., Arkenau, H.-T., Borazanci, E.H., Lopez, J.S., Pant, S., Schmid, P.*, et al.* (2016). Preliminary activity in the first in human study of the first-in-class fatty acid synthase (FASN) inhibitor, TVB-2640. J. Clin. Oncol. *34*, 2512-2512.

Dodge, G.J., Patel, A., Jaremko, K.L., McCammon, J.A., Smith, J.L., and Burkart, M.D. (2019). Structural and dynamical rationale for fatty acid unsaturation in *Escherichia coli*. Proc. Natl. Acad. Sci. USA *116*, 6775-6783.

Elad, N., Baron, S., Peleg, Y., Albeck, S., Grunwald, J., Raviv, G., Shakked, Z., Zimhony, O., and Diskin, R. (2018). Structure of Type-I Mycobacterium tuberculosis fatty acid synthase at 3.3 Å resolution. Nature Communications *9*, 3886.

Emsley, P., Lohkamp, B., Scott, W.G., and Cowtan, K. (2010). Features and development of *Coot*. Acta Crystallogr. D Biol. Crystallogr. *66*, 486-501.

Evans, P. (2005). Scaling and assessment of data quality. Acta Crystallogr. D Biol. Crystallogr. *62*, 72-82.

Flocco, M.M., and Mowbray, S.L. (1994). Planar stacking interactions of arginine and aromatic side-chains in proteins. J. Mol. Biol. *235*, 709-717.

Gansler, T.S., Hardman, W., Hunt, D.A., Schaffel, S., and Hennigar, R.A. (1997). Increased expression of fatty acid synthase (OA-519) in ovarian neoplasms predicts shorter survival. Hum. Pathol. *28*, 686-692.

Grininger, M. (2014). Perspectives on the evolution, assembly and conformational dynamics of fatty acid synthase type I (FAS I) systems. Curr. Opin. Struct. Biol. *25*, 49-56.

Hardwicke, M.A., Rendina, A.R., Williams, S.P., Moore, M.L., Wang, L., Krueger, J.A., Plant, R.N., Totoritis, R.D., Zhang, G., Briand, J., *et al.* (2014). A human fatty acid synthase inhibitor binds β-ketoacyl reductase in the keto-substrate site. Nat. Chem. Biol. *10*, 774-779.

Heil, C.S., Wehrheim, S.S., Paithankar, K.S., and Grininger, M. (2019). Fatty acid biosynthesis: Chain length regulation and control. ChemBioChem *0*.

Herbst, D.A., Townsend, C.A., and Maier, T. (2018). The architectures of iterative type I PKS and FAS. Nat. Prod. Rep. *35*, 1046-1069.

Hol, W.G. (1985). The role of the alpha-helix dipole in protein function and structure. Prog. Biophys. Mol. Biol. *45*, 149-195.

Johansson, P., Wiltschi, B., Kumari, P., Kessler, B., Vonrhein, C., Vonck, J., Oesterhelt, D., and Grininger, M. (2008). Inhibition of the fungal fatty acid synthase type I multienzyme complex. Proceedings of the National Academy of Sciences *105*, 12803-12808.

Kabsch, W. (2010). *XDS*. Acta Crystallogr. D Biol. Crystallogr. *66*, 125-132

Khandekar, M.J., Cohen, P., and Spiegelman, B.M. (2011). Molecular mechanisms of cancer development in obesity. Nature Reviews Cancer *11*, 886.

Khersonsky, O., and Tawfik, D.S. (2010). Enzyme Promiscuity: A Mechanistic and Evolutionary Perspective. Annu. Rev. Biochem. *79*, 471-505.

Kuhajda, F.P. (2006). Fatty Acid Synthase and Cancer: New Application of an Old Pathway. Cancer Res. *66*, 5977-5980.

Lee, W., and Engels, B. (2014). The Protonation State of Catalytic Residues in the Resting State of KasA Revisited: Detailed Mechanism for the Activation of KasA by Its Own Substrate. Biochemistry *53*, 919-931.

Leibundgut, M., Jenni, S., Frick, C., and Ban, N. (2007). Structural Basis for Substrate Delivery by Acyl Carrier Protein in the Yeast Fatty Acid Synthase. Science *316*, 288-290.

Liebschner, D., Afonine, P.V., Moriarty, N.W., Poon, B.K., Sobolev, O.V., Terwilliger, T.C., and Adams, P.D. (2017). Polder maps: improving OMIT maps by excluding bulk solvent. Acta Cryst (2017). D73, 148-157 [doi:10.1107/S2059798316018210], 1-10.

Lomakin, I.B., Xiong, Y., and Steitz, T.A. (2007). The Crystal Structure of Yeast Fatty Acid Synthase, a Cellular Machine with Eight Active Sites Working Together. Cell *129*, 319-332.

939 Luckner, S.R., Machutta, C.A., Tonge, P.J., and Kisker, C. (2009). Crystal
940 Structures of *Mycobacterium tuberculosis* KasA Show Mode of Action within
941 Cell Wall Biosynthesis and its Inhibition by Thiolactomycin. Structure/Folding
942 and Design *17*, 1004-1013.

943 Maier, T., Leibundgut, M., and Ban, N. (2008). The Crystal Structure of a
944 Mammalian Fatty Acid Synthase. Science *321*, 1315-1322.

945 Maier, T., Leibundgut, M., Boehringer, D., and Ban, N. (2010). Structure and
946 function of eukaryotic fatty acid synthases. Q. Rev. Biophys. *43*, 373-422.

947 Menendez, J.A., Vazquez-Martin, A., Ortega, F.J., and Fernandez-Real, J.M.
948 (2009). Fatty acid synthase: association with insulin resistance, type 2
949 diabetes, and cancer. Clin. Chem. *55*, 425-438.

950 Molnos, J., Gardiner, R., Dale, G.E., and Lange, R. (2003). A continuous
951 coupled enzyme assay for bacterial malonyl–CoA:acyl carrier protein
952 transacylase (FabD). Anal. Biochem. *319*, 171-176.

953 Murshudov, G.N., Skubák, P., Lebedev, A.A., Pannu, N.S., Steiner, R.A.,
954 Nicholls, R.A., Winn, M.D., Long, F., and Vagin, A.A. (2011). *REFMAC5* for
955 the refinement of macromolecular crystal structures. Acta Crystallogr. D Biol.
956 Crystallogr. *67*, 355-367.

957 Naggert, J., Witkowski, A., Wessa, B., and Smith, S. (1991). Expression in
958 Escherichia coli, purification and characterization of two mammalian
959 thioesterases involved in fatty acid synthesis. Biochem. J. *273*, 787-790.

960 Nguyen, P.L., Ma, J., Chavarro, J.E., Freedman, M.L., Lis, R., Fedele, G.,
961 Fiore, C., Qiu, W., Fiorentino, M., Finn, S.*, et al.* (2010). Fatty Acid Synthase
962 Polymorphisms, Tumor Expression, Body Mass Index, Prostate Cancer Risk,
963 and Survival. J. Clin. Oncol. *28*, 3958-3964.

964 Nguyen, T., Ishida, K., Jenke-Kodama, H., Dittmann, E., Gurgui, C.,
965 Hochmuth, T., Taudien, S., Platzer, M., Hertweck, C., and Piel, J. (2008).
966 Exploiting the mosaic structure of *trans*-acyltransferase polyketide synthases
967 for natural product discovery and pathway dissection. Nat. Biotechnol. *26*,
968 225-233.

969 Olsen, J.G., Kadziola, A., von Wettstein-Knowles, P., Siggaard-Andersen, M.,
970 and Larsen, S. (2001). Structures of beta-ketoacyl-acyl carrier protein
971 synthase I complexed with fatty acids elucidate its catalytic machinery.
972 Structure/Folding and Design *9*, 233-243.

973 Paiva, P., Sousa, S.r.F., Ramos, M.J., and Fernandes, P.A. (2018).
974 Understanding the Catalytic Machinery and the Reaction Pathway of the
975 Malonyl-Acetyl Transferase Domain of Human Fatty Acid Synthase. ACS
976 Catalysis *8*, 4860-4872.

977 Pandey, P.R., Liu, W., Xing, F., Fukuda, K., and Watabe, K. (2012). Anti-
978 Cancer Drugs Targeting Fatty Acid Synthase (FAS). Recent Pat. Anticancer
979 Drug Discov. *7*, 185-197.

980 Pappenberger, G., Benz, J., Gsell, B., Hennig, M., Ruf, A., Stihle, M., Thoma,
981 R., and Rudolph, M.G. (2010). Structure of the Human Fatty Acid Synthase
982 KS–MAT Didomain as a Framework for Inhibitor Design. J. Mol. Biol. *397*,
983 508-519.

984 Pemble, C.W., Johnson, L.C., Kridel, S.J., and Lowther, W.T. (2007). Crystal
985 structure of the thioesterase domain of human fatty acid synthase inhibited by
986 Orlistat. Nature Structural & Molecular Biology *14*, 704-709.

987 Ploskoń, E., Arthur, C.J., Evans, S.E., Williams, C., Crosby, J., Simpson, T.J.,
988 and Crump, M.P. (2008). A Mammalian Type I Fatty Acid Synthase Acyl
989 Carrier Protein Domain Does Not Sequester Acyl Chains. J. Biol. Chem. *283*,
990 518-528.

991 Rangan, V.S., and Smith, S. (1997). Alteration of the Substrate Specificity of
992 the Malonyl-CoA/Acetyl-CoA: Acyl Carrier Protein *S*-Acyltransferase Domain
993 of the Multifunctional Fatty Acid Synthase by Mutation of a Single Arginine
994 Residue. J. Biol. Chem. *272*, 11975-11978.

995 Rashid, A., Pizer, E.S., Moga, M., Milgraum, L.Z., Zahurak, M., Pasternack,
996 G.R., Kuhajda, F.P., and Hamilton, S.R. (1997). Elevated expression of fatty
997 acid synthase and fatty acid synthetic activity in colorectal neoplasia. The
998 American journal of pathology *150*, 201-208.

999 Rittner, A., Paithankar, K.S., Drexler, D.J., Himmler, A., and Grininger, M.
1000 (2019). Probing the modularity of megasynthases by rational engineering of a
1001 fatty acid synthase Type I. Protein Sci. *28*, 414-428.

1002 Rittner, A., Paithankar, K.S., Huu, K.V., and Grininger, M. (2018).
1003 Characterization of the Polyspecific Transferase of Murine Type I Fatty Acid
1004 Synthase (FAS) and Implications for Polyketide Synthase (PKS) Engineering.
1005 ACS Chem. Biol. *13*, 723-732.

1006 Rossini, E., Gajewski, J., Klaus, M., Hummer, G., and Grininger, M. (2018).
1007 Analysis and engineering of substrate shuttling by the acyl carrier protein
1008 (ACP) in fatty acid synthases (FASs). Chem. Commun. *68*, 501.

1009 Semenkovich, C.F., Coleman, T., and Fiedorek, F.T. (1995). Human fatty acid
1010 synthase mRNA: tissue distribution, genetic mapping, and kinetics of decay
1011 after glucose deprivation. J. Lipid Res. *36*, 1507-1521.

1012 Smith, S., and Stern, A. (1983). The Effect of Aromatic CoA Esters on Fatty
1013 Acid Synthetase: Biosynthesis of *ω*-Phenyl Fatty Acids. Arch. Biochem.
1014 Biophys. *222*, 259-265.

1015 Smith, S., and Tsai, S.-C. (2007). The type I fatty acid and polyketide
1016 synthases: a tale of two megasynthases. Nat. Prod. Rep. *24*, 1041-1072.

1017 Sztain, T., Bartholow, T.G., Orcid, J.A.M., and Orcid, M.D.B. (2019). Shifting
1018 the Hydrolysis Equilibrium of Substrate Loaded Acyl Carrier Proteins.
1019 Biochemistry, 1-4.

1020 Uhlén, M., Fagerberg, L., Hallström, B.M., Lindskog, C., Oksvold, P.,
1021 Mardinoglu, A., Sivertsson, Å., Kampf, C., Sjöstedt, E., Asplund, A.*, et al.*
1022 (2015). Tissue-based map of the human proteome. Science *347*, 1260419.

1023 Vagin, A., and Teplyakov, A. (1997). *MOLREP*: an Automated Program for
1024 Molecular Replacement. J. Appl. Crystallogr. *30*, 1022-1025.

1025 von Wettstein-Knowles, P., Olsen, J.G., McGuire, K.A., and Henriksen, A.
1026 (2006). Fatty acid synthesis. Role of active site histidines and lysine in Cys-
1027 His-His-type beta-ketoacyl-acyl carrier protein synthases. FEBS J. *273*, 695-
1028 710.

1029 Wang, J., Soisson, S.M., Young, K., Shoop, W., Kodali, S., Galgoci, A.,
1030 Painter, R., Parthasarathy, G., Tang, Y.S., Cummings, R.*, et al.* (2006).
1031 Platensimycin is a selective FabF inhibitor with potent antibiotic properties.
1032 Nature *441*, 358-361.

1033 White, S.W., Zheng, J., Zhang, Y.-M., and Rock, C.O. (2005). The Structural
1034 Biology of Type II Fatty Acid Biosynthesis. Annu. Rev. Biochem. *74*, 791-831.

1035 Winn, M.D., Isupov, M.N., and Murshudov, G.N. (2001). Use of TLS
1036 parameters to model anisotropic displacements in macromolecular
1037 refinement. Acta Crystallographica Section D *57*, 122-133.

1038 Witkowski, A., Joshi, A.K., and Smith, S. (1997). Characterization of the
1039 Interthiol Acyltransferase Reaction Catalyzed by the *β*-Ketoacyl Synthase
1040 Domain of the Animal Fatty Acid Synthase. Biochemistry *36*, 16338-16344.

1041 Zhang, W., Chakravarty, B., Zheng, F., Gu, Z., Wu, H., Mao, J., Wakil, S.J.,
1042 and Quiocho, F.A. (2011). Crystal structure of FAS thioesterase domain with
1043 polyunsaturated fatty acyl adduct and inhibition by dihomo-γ-linolenic acid.
1044 Proc. Natl. Acad. Sci. U. S. A. *108*, 15757-15762.
1045

1046